Engineering 19 (2022) 105–116

Contents lists available at ScienceDirect

Engineering

journal homepage: www.elsevier.com/locate/eng

Research
Intelligent Manufacturing—Article

# 3D Microdisplacement Monitoring of Large Aircraft Assembly with Automated *In Situ* Calibration

Zhenyuan Jia, Bing Liang, Wei Liu *, Kun Liu, Jianwei Ma

*School of Mechanical Engineering, Dalian University of Technology, Dalian 116024, China*

ARTICLE INFO

*Article history:*
Received 3 April 2020
Revised 20 July 2020
Accepted 21 February 2021
Available online 2 November 2021

*Keywords:*
Aircraft manufacture
Assembly
Calibration
Condition monitoring
Displacement measurement

ABSTRACT

Three-dimensional (3D) microdisplacement monitoring plays a crucial role in the assembly of large aircraft. This paper presents a broadly applicable high-precision online 3D microdisplacement monitoring method and system based on proximity sensors as well as a corresponding *in situ* calibration method, which can be applied under various extreme working conditions encountered in the aircraft assembly process, such as compact and obstructed spaces. A 3D monitoring model is first established to achieve 3D microdisplacement monitoring based only on the one-dimensional distances measured by proximity sensors, which concerns the extrinsic sensor parameters, such as the probe base point (PBP) and the unit displacement vector (UDV). Then, a calibration method is employed to obtain these extrinsic parameters with high precision by combining spatial transformation principles and weighted optimization. Finally, calibration and monitoring experiments performed for a tailplane assembly process are reported. The calibration precision for the PBP is better than ±10 μm in the *X* and *Y* directions and ±2 μm in the *Z* direction, and the calibration precision for the UDV is better than 0.07°. Moreover, the accuracy of the 3D microdisplacement monitoring system can reach ±15 μm. In general, this paper provides new insights into the modeling and calibration of 3D microdisplacement monitoring based on proximity sensors and a precise, efficient, and low-cost technical means for performing related measurements in compact spaces during the aircraft assembly process.



## 1. Introduction

Aircraft assembly is one of the most important processes in aircraft production. Because of the extreme complexity of the assembly process, including structural support [1], component alignment [2], surface normal measurement of the drilling parts [3], and posture adjustment without clearance [4], this process accounts for more than 50% of the aircraft manufacturing workload. Assembly tooling to support and position the aeronautical components ensures the quality of aircraft assembly to a great extent. However, due to the inevitable stress concentrations and vibrations experienced during assembly, microdisplacements of the key positioners of the assembly tooling system will occur, which may result in gaps and other deformations of the assembled products. With the current trend toward intelligent manufacturing [5], for the realization of self-perception of measurement information, self-decision-making with regard to assembly processes and self-execution of assembly operations in aircraft assembly, structural health monitoring has become indispensable in the field of aerospace engineering [6]. Thus, in the process of assembling large aircraft, high-precision and high-efficiency microdisplacement monitoring of the assembly tooling is playing an increasingly crucial role in improving the accuracy and reliability of large aircraft assembly.

High-precision measurement methods have been adopted in assembly tooling microdisplacement inspection. Light detection and ranging (LiDAR) technology [7–9] is widely used in assembly preparation and assembly station coordination tasks, such as assembly station positioning and aircraft component prepositioning. The precision can reach 100 μm with an ultra large measurement range of more than 100 m. Laser trackers [10–12] are widely used in offline displacement inspection and *in situ* intermittent inspection of assembly tooling. Their measurement range spans 10–60 m, and their measurement precision can reach ±(15 μm + 6 μm·m$^{-1}$), making these instruments the benchmark for position inspections. For three-dimensional (3D) reconstruction of the key profile on assembly tooling, 3D structured scanning

* Corresponding author.
*E-mail address:* Lw2007@dlut.edu.cn (W. Liu).

https://doi.org/10.1016/j.eng.2021.02.023

[13,14] is widely used to achieve high accuracy within a small field of view. The accuracy of 3D structured scanning equipment can be as high as 12 μm within a field of view of 35 mm × 40 mm. Regarding industrial photogrammetry [15–17], its high precision of up to ±(14 μm + 14 μm·m$^{-1}$) and high efficiency enable the precise and fast displacement inspection of key points on an assembly tooling profile. However, various extreme working conditions are often encountered in the aircraft assembly process; a typical example is the multistep assembly process of the tailplane of an aircraft, wherein the various tailplane parts, the complex assembly tooling structures, the large number of manual operations, the compact measurement space (as small as 5 mm × 10 mm × 15 mm or even smaller) and the high precision requirements (±76 μm in a range of 7 m) present serious difficulties for the online microdisplacement monitoring of the positioners of the assembly tooling. Thus, it is necessary to adopt an online monitoring method that simultaneously considers accuracy, efficiency, volume, and cost to determine the position accuracy of the assembly tooling positioners. In terms of the completeness of the measurement information, due to the limitations of volume, obstruction, and measurement frequency, it is difficult for any existing single set of integrated equipment to obtain all relevant information simultaneously. From the efficiency perspective, the dynamic performance of laser trackers and 3D structured scanning equipment is not sufficient to meet the needs of online monitoring. Concerning cost, laser trackers, and industrial cameras are too expensive for it to be feasible to overcome the problem of incomplete measurement information due to complex working conditions by simply increasing the amount of equipment used. Therefore, considering the compact space and obstruction of assembly tooling due to components and artificial sources, the measurement means mentioned above generally fail to meet the requirements of online microdisplacement monitoring in terms of high precision, high efficiency, and low cost.

Proximity sensors [18–20] are widely used in high-precision distance inspection in various fields because of their advantages of high precision, compact volume, light weight, fast response, and low cost. Similarly, in aircraft assembly, these sensors can be positioned in compact spaces and used to monitor the one-dimensional (1D) distances to the positioners of an assembly tooling system. Then, to acquire the 3D displacements of the positioners, a measurement model for transforming 1D distance information into 3D information is necessary, which is directly related to the precision of 3D monitoring. Most current research is focusing on measurement processes based on proximity sensors manipulated by high-precision actuators, such as those on a coordinate measuring machine (CMM) or a robot. In this case, the 3D measurement model can be established by combining the kinematic information of the actuators with the 1D distance measurement information of the proximity sensors. However, in an online monitoring process based on fixed sensors, only distance information can be obtained, and consequently, the 3D modeling method used for a CMM or robot cannot be directly applied for the modeling and calibration of the 3D monitoring scenario considered in this paper.

The motivation of this work is to propose a broadly applicable 3D microdisplacement monitoring method based on proximity sensors that can be applied under various extreme working conditions encountered in the aircraft assembly process, such as compact and obstructed spaces. Meanwhile, an automated *in situ* calibration method for the 3D microdisplacement model is proposed that can calculate the extrinsic parameters of the proximity sensors, including the probe base point (PBP) and unit displacement vector (UDV), with high precision and thus facilitate the precise 3D microdisplacement monitoring process. The importance and originality of this study are that it provides new insights into the modeling and calibration of 3D microdisplacement monitoring based on proximity sensors and a precise, efficient, and low-cost technical means of conducting related measurements in compact spaces during the aircraft assembly process.

The rest of this paper is organized as follows. Section 2 reviews the previous work related to this paper. Section 3 describes the 3D microdisplacement monitoring method and system. Section 4 details the proposed automated *in situ* extrinsic calibration strategy. In Section 5, calibration experiments and monitoring experiments are presented. Finally, the paper is concluded in Section 6.

## 2. Related works

Scholars in various fields have carried out many studies on establishing 3D measurement models and methods for calibrating extrinsic sensor parameters in order to transform sensor measurements into 3D measurements in the world coordinate system (WCS).

### 2.1. Establishment of the 3D measurement model

In terms of 3D measurement models, vision-based, proximity-sensor-based, and multisensor-based methods have all been extensively studied. Researchers have mainly used the intrinsic measurement characteristics of sensors and positional reference information to establish 3D measurement models.

An et al. [9] developed a 3D laser ranging system based on a camera and a two-dimensional (2D) laser rangefinder, with an average calibration error of 0.9875 pixels. Tests indicated that the laser ranging system showed good performance for both outdoor and indoor applications. Uekita and Takaya [21] developed a measurement system for the on-machine diameter measurement of a steam turbine rotor based on a touch-trigger probe and a laser tracker, with a maximum discrepancy of 0.028 mm. Kim et al. [22] proposed a novel 6-degree-of-freedom (6-DOF) measurement system composed of a camera and 1D laser sensors. Experiments were performed to validate the performance of the system and demonstrated accuracies of 4 mm and 0.5° in a 30 m measurement range. Liu et al. [23] developed a 3D sensing system based on three orthogonal microscopic cameras to realize the high-precision assembly of two components. Experiments indicated that the alignment errors were less than ±0.1° in terms of orientation and ±2 μm in terms of position. Kim et al. [24] developed a long-range motion-sensing system based on three 1D laser sensors, infrared markers, and vision cameras, with an accuracy of 3 mm at a 30 m distance.

### 2.2. Extrinsic parameter calibration

For extrinsic parameter calibration for 3D measurement models based on 1D or 2D sensors, spatial transformation theory and benchmark data constraints have often been employed.

Zapico et al. [25] proposed an extrinsic calibration method to facilitate the transformation of coordinates captured by a 1D sensor integrated into a CMM with respect to the coordinate system of the CMM. The diameters of spheres were measured with residuals of less than 8 μm. Liu et al. [26] elaborated a novel calibration method for achieving 3D measurement by means of a single 1D eddy current displacement sensor. Experiments showed that the average measurement accuracy was 21.2 μm. Bi et al. [27,28] developed a noncontact coordinate measurement system based on a 1D laser displacement sensor, in which the beam direction of the sensor was calibrated by means of a standard sphere. Based on the calibration results, the measurement uncertainty of the measurement system was approximately 30 μm. Wu and Ren

[29] proposed a hand–eye calibration method to solve for the kinematic base frame of a robot, in which the unknown extrinsic parameters of the base frame were calculated by minimizing the coordinate conversion errors. Guo et al. [30] proposed a novel measurement method based on a laser displacement sensor. The particle swarm optimization algorithm and the least squares algorithm were combined to calibrate the kinematic parameters of a robot. Experimental results indicated that the mean of the estimated positioning errors could be reduced to 0.845 mm. Sharifzadeh et al. [31] presented a semiautomatic hand–eye calibration strategy based on a single plane artifact, which required only four manually scanned lines. The calibration strategy was demonstrated to be simple, robust and accurate, with an error of 0.066 mm between the reconstructed 3D points and the corresponding fitted plane; hence, this is a suitable low-cost approach that is easy to implement for many industrial applications of robot-deployed laser scanning. Zou and Lan [32] proposed a hand–eye calibration method for laser vision systems based on deep reinforcement learning. Moreover, a reinforcement learning framework was adopted for network training to handle the issue of insufficient training data. Experimental results showed that the proposed method enabled distinct improvements in precision and stability, with a positioning error of less than 0.8 mm.

### 2.3. Discussion

For a more intuitive understanding of state-of-the-art 3D monitoring methods based on laser trackers, 2D cameras and 1D proximity sensors, a comparison of these multi-DOF sensors is summarized in Table 1 [10,11,21–32]. It can be seen that the proposed method can support high-efficiency inspection in a compact space and perfectly satisfy the requirements for assembly tooling inspection with an accuracy of ±0.076 mm.

In general, to establish a 3D measurement model based on 2D sensors such as cameras, spatial transformation principles are often employed for extrinsic parameter calibration. Multidimensional information can be measured and applied for calibration to provide additional constraints and enhance the calibration precision. To establish a 3D measurement model based on 1D sensors such as proximity sensors, optimization methods based on scalar constraints (e.g., distance and diameter) are usually adopted. In addition to the dimensional information of the measured distance, a high-precision motion mechanism is needed to drive the sensor, thereby completing the process of calibrating the extrinsic parameters.

For 3D microdisplacement monitoring during the assembly of large aircraft, proximity sensors are fixed at various positions on the assembly tooling. Local microdistances are measured at the millimeter level or even at the micron level. Then, these distances are transformed into displacements in the WCS for aircraft assembly (which measures several meters in length, width, and height). The errors of these local microdistances can be easily amplified during the transformation from the local coordinate system to the WCS, resulting in a significant reduction in calibration accuracy. Thus, we need to combine the calibration methods for 2D sensors and 1D sensors to achieve high-precision calibration of the fixed sensors. This purpose can be achieved with the calibration method proposed in this paper.

## 3. 3D microdisplacement monitoring method

In the assembly of large aircraft, forced assembly and vibrations will inevitably occur due to dimensional errors and thermal deformations of the components, drilling operations, operator errors, and so forth, seriously affecting the accuracy of the assembly process. Because the assembly tooling system is of key importance in aircraft part positioning, online 3D microdisplacement monitoring of the core positioners of the assembly tooling is indispensable.

Fig. 1 shows the proposed 3D microdisplacement monitoring system based on distributed proximity sensors and a computer. Each sensor operates in its own sensor coordinate system (SCS), where $\delta$ is the measured distance that will finally be acquired by the computer.

Since the distance $\delta$ measured by a proximity sensor is a scalar value, a 3D measurement model is necessary to obtain the 3D coordinates of the measured points. To this end, the extrinsic parameters of each proximity sensor are introduced, including the PBP and the UDV. To transform the measured distances into displacements in the WCS, suppose that the PBP $\boldsymbol{O}^{\mathrm{W}}$ and the UDV $\boldsymbol{t}^{\mathrm{W}}$ of a sensor in the WCS can be expressed as follows:

$$\boldsymbol{O}^{\mathrm{W}} = \begin{bmatrix} O_X^{\mathrm{W}} & O_Y^{\mathrm{W}} & O_Z^{\mathrm{W}} \end{bmatrix}^{\mathrm{T}} \tag{1}$$

$$\boldsymbol{t}^{\mathrm{W}} = \begin{bmatrix} t_X^{\mathrm{W}} & t_Y^{\mathrm{W}} & t_Z^{\mathrm{W}} \end{bmatrix}^{\mathrm{T}} \tag{2}$$

where $O_X^{\mathrm{W}}$, $O_Y^{\mathrm{W}}$, $O_Z^{\mathrm{W}}$, $t_X^{\mathrm{W}}$, $t_Y^{\mathrm{W}}$, and $t_Z^{\mathrm{W}}$ are the six extrinsic sensor parameters projected from $\boldsymbol{O}^{\mathrm{W}}$ and $\boldsymbol{t}^{\mathrm{W}}$ to the $X$, $Y$, and $Z$ axes of the WCS. There is the following implicit constraint:

$$\| \boldsymbol{t}^{\mathrm{W}} \|_2 = \left(t_X^{\mathrm{W}}\right)^2 + \left(t_Y^{\mathrm{W}}\right)^2 + \left(t_Z^{\mathrm{W}}\right)^2 = 1 \tag{3}$$

Then, the 3D measurement model of this sensor in the WCS can be expressed as follows:

$$\boldsymbol{P}^{\mathrm{W}} = \begin{pmatrix} x^{\mathrm{W}} & y^{\mathrm{W}} & z^{\mathrm{W}} \end{pmatrix}^{\mathrm{T}} = \boldsymbol{O}^{\mathrm{W}} + \delta \boldsymbol{t}^{\mathrm{W}} \tag{4}$$

where $\boldsymbol{P}^{\mathrm{W}} = \begin{pmatrix} x^{\mathrm{W}} & y^{\mathrm{W}} & z^{\mathrm{W}} \end{pmatrix}^{\mathrm{T}}$ is the point on the positioner to be measured in the WCS, and $x^{\mathrm{W}}$, $y^{\mathrm{W}}$, and $z^{\mathrm{W}}$ are the coordinate components of point $\boldsymbol{P}^{\mathrm{W}}$ on the $X$, $Y$, and Z axes, respectively. Thus, the monitoring model is established based on the extrinsic sensor parameters.

The key points to be monitored on the core positioners of the aircraft tooling system are highly scattered, so sensors are distributed in corresponding positions. The structure of the microdisplacement monitoring system is shown in Fig. 2. The sensors are

**Table 1**
Comparison of multi-DOF sensors for 3D monitoring.

| Methods | Main sensing devices | Measurement mode | Accuracy (at 7 m) | Remark |
|---|---|---|---|---|
| Refs. [10,11,29] | 3D laser trackers | Optical, noncontact | < 0.100 mm | High accuracy, low efficiency, and invalid measurement of obstructed objects |
| Refs. [22–24,31,32] | 2D cameras or laser scanners | Optical, noncontact | ~0.070–1.000 mm | Low accuracy, high efficiency, and invalid measurement of obstructed objects |
| Refs. [21,25–28,30] | 1D movable proximity sensors | Optical, noncontact or contact | ~0.010–0.100 mm | High accuracy, high efficiency, sensors driven by manipulators, and equipment volume too large to permit measurement in a compact space |
| Proposed method | 1D fixed proximity sensors | Magnetic, noncontact | < 0.076 mm | High accuracy, high efficiency, compact sensor volume, and sensors distributed in the measurement space |

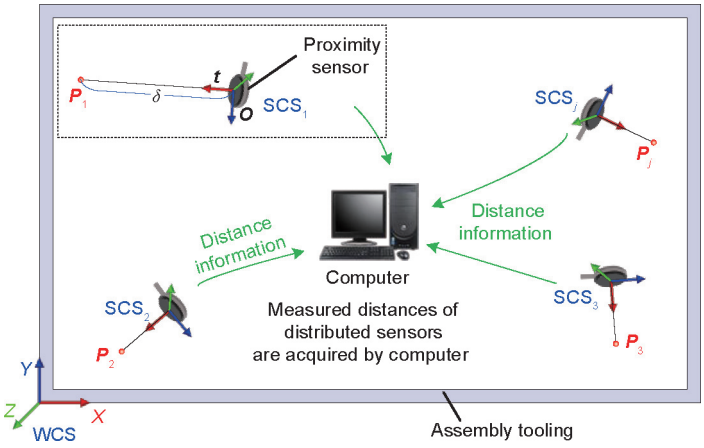


**Fig. 1.** 3D microdisplacement monitoring system and principle. $\delta$: the measured distance; ***O***: PBP; ***t***: UDV; $\boldsymbol{P}_j$ ($j$ = 1, 2, 3…): the measured point of the $j$th sensor; $SCS_j$ ($j$ = 1, 2, 3…): the coordinate system of the $j$th sensor; $j$: the number of the sensor.

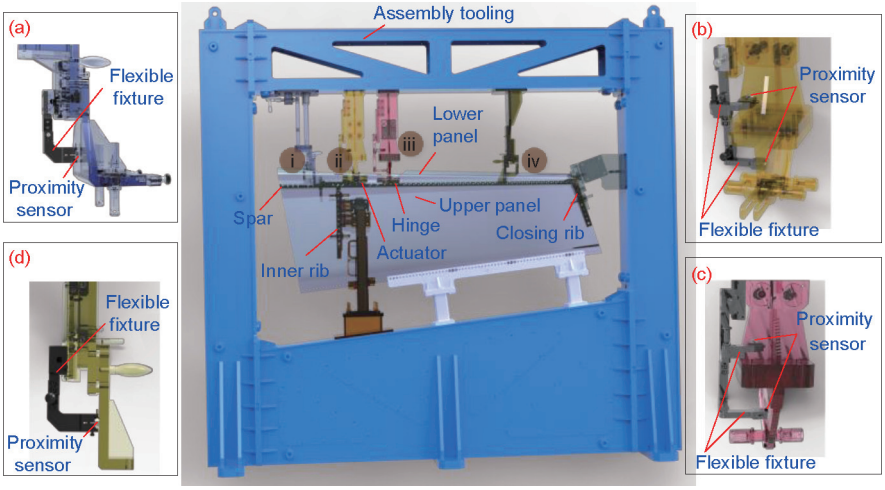


**Fig. 2.** 3D microdisplacement monitoring of an assembly tooling system. (a) spar positioner; (b) actuator positioner; (c) hinge positioner; (d) spar auxiliary positioner.

distributed and fixed in specific positions by the designed flexible fixtures. Then, the measured distances are acquired and used to calculate the 3D microdisplacements.

As shown in Fig. 2, a monitoring system based on proximity sensors is adopted to monitor the assembly tooling system for the assembly of a tailplane. This monitoring system consists of dozens of proximity sensors for monitoring different positions. For practical monitoring purposes, it is necessary to calibrate the extrinsic parameters of each of the distributed proximity sensors. Thus, the following calibration method is proposed.

## 4. Calibration method

The calibration strategy consists of four parts: solving for the transformation matrices of the coordinate motions, establishing point-to-surface constraints, performing weighted optimization of the calibration results, and designing an automated calibration process. First, the calibration plane is placed in various positions, and the corresponding relations are calculated by solving for the transformation matrices. Second, point-to-surface constraints are established based on the transformation matrices as the foundation for the optimization objectives. Then, weighted optimization based on sample equalization is carried out. Finally, an automated calibration process is designed to complete the entire calibration process.

The calibration strategy and process are illustrated in Fig. 3.

An industrial robot with a calibration end effector and a laser tracker are adopted to calibrate the sensor extrinsic parameters. The calibration end effector consists of a high-precision 6-DOF motion platform and a calibration plane. The calibration plane coordinate system (CPCS) is established based on the coordinate system of the 6-DOF motion platform itself. The WCS is the basic coordinate system of the aircraft assembly process and is established by the laser tracker, and the CPCS is the working coordinate system of the calibration process and is established by the 6-DOF motion platform. The calibration process is performed in the CPCS, in which the calibration plane moves to different poses driven by the 6-DOF motion platform. Then, point-to-surface constraints are established between the coordinates of the measuring points obtained by the proximity sensor and the calibration plane. The extrinsic parameters (PBP and UDV) of the proximity sensor that appear in the constraints are determined in the CPCS. Finally, several holes are employed as datum points to facilitate the

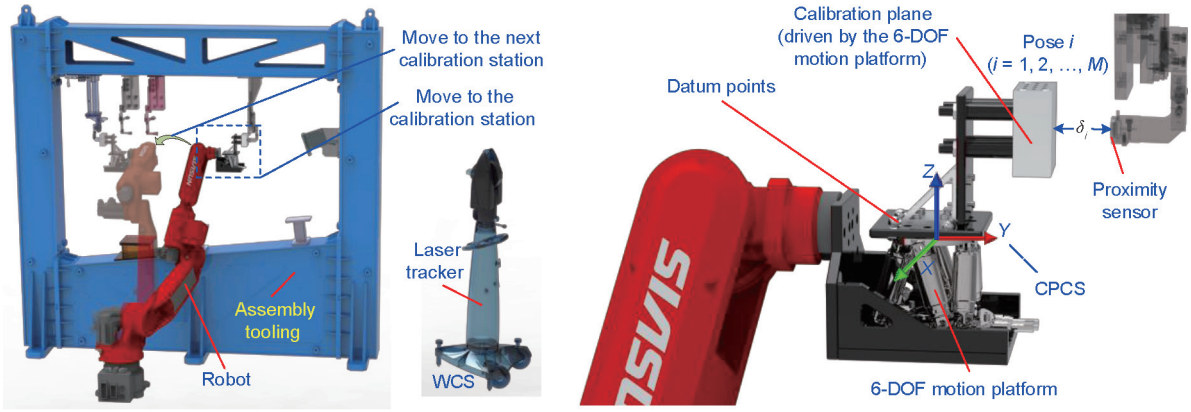


**Fig. 3.** Calibration strategy and process: (a) calibration process, (b) calibration end effector and calibration strategy. *i*: the *i*th pose of the calibration plane after the *i*th motion of the 6-DOF motion platform; $\delta_i$: the distance measured by the proximity sensor after the *i*th motion of the calibration plane; *M*: the number of calibration samples collected in the process of calibrating a proximity sensor; CPCS: calibration plane coordinate system.

transformation between the CPCS and the WCS based on the laser tracker. The calibration process is automatically repeated by the industrial robot to calibrate the next sensor until all sensors are calibrated.

### 4.1. Transformation matrices of coordinate motions

To ensure the subsequent accuracy of the constraints and the calibration process, accurate plane equations are necessary. In the CPCS, the order of the motion of the calibration plane is specified as $\alpha \to \beta \to \gamma \to l \to m \to n$, where $\alpha$, $\beta$, and $\gamma$ are the rotation angles around the *X*, *Y*, and *Z* axes, respectively; and *l*, *m*, and *n* are the translation distances along the *X*, *Y*, and *Z* axes of the 6-DOF motion platform, respectively, as shown in Fig. 3(b).

Then, after the *i*th motion, the 3D coordinates of the points on the calibration plane in the CPCS, $\boldsymbol{P}_i^{\mathrm{CP}}$, can be expressed as:

$$\boldsymbol{P}_i^{\mathrm{CP}} = \begin{pmatrix} x_i^{\mathrm{CP}} & y_i^{\mathrm{CP}} & z_i^{\mathrm{CP}} \end{pmatrix}^{\mathrm{T}} = \boldsymbol{R}_{0\to i}^{\mathrm{CP}} \begin{pmatrix} x_0^{\mathrm{CP}} & y_0^{\mathrm{CP}} & z_0^{\mathrm{CP}} \end{pmatrix}^{\mathrm{T}} + \boldsymbol{T}_{0\to i}^{\mathrm{CP}}, \ (i = 1, 2, \ldots, M) \tag{5}$$

where *M* is the number of calibration samples collected in the process of calibrating a proximity sensor; $x_i^{\mathrm{CP}}$, $y_i^{\mathrm{CP}}$, and $z_i^{\mathrm{CP}}$ are the coordinate components of point $\boldsymbol{P}_i^{\mathrm{CP}}$ on the *X*, *Y*, and *Z* axes in the CPCS; $\boldsymbol{P}_0^{\mathrm{CP}} = \begin{pmatrix} x_0^{\mathrm{CP}} & y_0^{\mathrm{CP}} & z_0^{\mathrm{CP}} \end{pmatrix}^{\mathrm{T}}$ represents the 3D coordinates of the point on the initial calibration plane (denoted by pose 0); $x_0^{\mathrm{CP}}$, $y_0^{\mathrm{CP}}$, and $z_0^{\mathrm{CP}}$ are the coordinate components of point $\boldsymbol{P}_0^{\mathrm{CP}}$ on the *X*, *Y*, and *Z* axes in the CPCS respectively; $\boldsymbol{R}_{0\to i}^{\mathrm{CP}}$ and $\boldsymbol{T}_{0\to i}^{\mathrm{CP}}$ are the rotation and translation matrices, respectively. Then, the transformation of the calibration plane from pose 0 to pose *i* in the CPCS can be expressed as:

$$\boldsymbol{R}_{0\to i}^{\mathrm{CP}} = \begin{pmatrix} 1 & 0 & 0 \\ 0 & \cos\alpha & -\sin\alpha \\ 0 & \sin\alpha & \cos\alpha \end{pmatrix} \begin{pmatrix} \cos\beta & 0 & \sin\beta \\ 0 & 1 & 0 \\ -\sin\beta & 0 & \cos\beta \end{pmatrix} \begin{pmatrix} \cos\gamma & -\sin\gamma & 0 \\ \sin\gamma & \cos\gamma & 0 \\ 0 & 0 & 1 \end{pmatrix} \tag{6}$$

$$\boldsymbol{T}_{0\to i}^{\mathrm{CP}} = \begin{pmatrix} l & m & n \end{pmatrix}^{\mathrm{T}} \tag{7}$$

### 4.2. Point-to-surface constraints

Because the coordinates of the points measured by a proximity sensor always satisfy the calibration plane equation, point-to-surface constraints are employed to determine the extrinsic parameters of the proximity sensors in this paper.

The plane equation at the initial position in the CPCS should be known in advance and can be measured on a CMM, and the corresponding spatial equation is obtained as follows:

$$\boldsymbol{N}_0^{\mathrm{CP}} \begin{bmatrix} \boldsymbol{P}_0^{\mathrm{CP}} \\ 1 \end{bmatrix} = 0 \tag{8}$$

where $\boldsymbol{N}_0^{\mathrm{CP}}$ is the parameter vector of the calibration plane at the initial position (pose 0).

When the calibration plane moves, a new relationship is established.

$$\boldsymbol{N}_i^{\mathrm{CP}} \begin{bmatrix} \boldsymbol{P}_i^{\mathrm{CP}} \\ 1 \end{bmatrix} = 0 \tag{9}$$

where $\boldsymbol{N}_i^{\mathrm{CP}}$ is the parameter vector of the calibration plane at pose *i*.

According to Eq. (5), we can obtain

$$\boldsymbol{P}_i^{\mathrm{CP}} = \begin{bmatrix} \boldsymbol{R}_{0\to i}^{\mathrm{CP}} & \boldsymbol{T}_{0\to i}^{\mathrm{CP}} \end{bmatrix} \begin{bmatrix} \boldsymbol{P}_0^{\mathrm{CP}} \\ 1 \end{bmatrix} \tag{10}$$

By substituting Eq. (10) into Eq. (8), we can obtain

$$\boldsymbol{N}_0^{\mathrm{CP}} \begin{bmatrix} \left(\boldsymbol{R}_{0\to i}^{\mathrm{CP}}\right)^{-1} \boldsymbol{P}_i^{\mathrm{CP}} - \left(\boldsymbol{R}_{0\to i}^{\mathrm{CP}}\right)^{-1} \boldsymbol{T}_{0\to i}^{\mathrm{CP}} \\ 1 \end{bmatrix} = 0 \tag{11}$$

where $\left(\boldsymbol{R}_{0\to i}^{\mathrm{CP}}\right)^{-1}$ represents the inverse matrix of $\boldsymbol{R}_{0\to i}^{\mathrm{CP}}$.

Upon decomposing the matrix, Eq. (11) can be expressed as:

$$\boldsymbol{N}_0^{\mathrm{CP}} \begin{bmatrix} \left(\boldsymbol{R}_{0\to i}^{\mathrm{CP}}\right)^{-1} & -\left(\boldsymbol{R}_{0\to i}^{\mathrm{CP}}\right)^{-1} \boldsymbol{T}_{0\to i}^{\mathrm{CP}} \\ 0 & 1 \end{bmatrix} \begin{bmatrix} \boldsymbol{P}_i^{\mathrm{CP}} \\ 1 \end{bmatrix} = 0 \tag{12}$$

Combining Eqs. (9) and (12), we can obtain:

$$\boldsymbol{N}_i^{\mathrm{CP}} = \boldsymbol{N}_0^{\mathrm{CP}} \begin{pmatrix} \left(\boldsymbol{R}_{0\to i}^{\mathrm{CP}}\right)^{-1} & -\left(\boldsymbol{R}_{0\to i}^{\mathrm{CP}}\right)^{-1} \boldsymbol{T}_{0\to i}^{\mathrm{CP}} \\ 0 & 1 \end{pmatrix} \tag{13}$$

When the calibration plane moves to pose *i*, Eq. (4) can be expressed in the CPCS as follows:

$$\boldsymbol{P}_i^{\mathrm{CP}} = \boldsymbol{O}^{\mathrm{CP}} + \delta_i \boldsymbol{t}^{\mathrm{CP}} \tag{14}$$

where $\delta_i$ is the distance measured by the proximity sensor after the *i*th motion of the calibration plane, and $\boldsymbol{O}^{\mathrm{CP}}$ and $\boldsymbol{t}^{\mathrm{CP}}$ are the PBP and UDV of the proximity sensor in the CPCS, respectively.

Because the measurement point $\boldsymbol{P}_i^{\mathrm{CP}}$ is on the calibration plane, it holds that Eq. (14) obeys Eq. (9). When the calibration plane moves to different positions (pose $i$, $i$ = 1, 2, ..., $M$), by substituting Eq. (13) and Eq. (14) into Eq. (9), a corresponding set of constraints can be obtained as follows:

$$\boldsymbol{N}_0^{\mathrm{CP}}\begin{pmatrix}\left(\boldsymbol{R}_{0\to i}^{\mathrm{CP}}\right)^{-1} & -\left(\boldsymbol{R}_{0\to i}^{\mathrm{CP}}\right)^{-1}\boldsymbol{T}_{0\to i}^{\mathrm{CP}}\\ 0 & 1\end{pmatrix}\begin{bmatrix}\boldsymbol{O}^{\mathrm{CP}}+\delta_i\boldsymbol{t}^{\mathrm{CP}}\\ 1\end{bmatrix}=0,\ (i=1,2,...,M) \tag{15}$$

### 4.3. Weighted optimization

It can be easily seen that Eq. (15) is an overdetermined linear system of equations with no theoretical solution. Moreover, because of the various errors that arise in actual tests, it is almost impossible for the equalities in Eq. (15) to be satisfied. Thus, an allowable minimal constant error $\varepsilon$, such as $\varepsilon$ = 0.1, needs to be introduced to achieve an approximate solution. For brevity, let $\boldsymbol{s}^{\mathrm{CP}}=\left(\boldsymbol{O}^{\mathrm{CP}},\boldsymbol{t}^{\mathrm{CP}}\right)$, and let $\boldsymbol{f}(\boldsymbol{s}^{\mathrm{CP}})$ represent the left side of Eq. (15). Eq. (15) can then be modified as follows:

$$\|\boldsymbol{f}(\boldsymbol{s}^{\mathrm{CP}})\|_2\le\varepsilon \tag{16}$$

Due to the different contributions of each calibration sample to the error of the approximate solution, weight coefficients $\boldsymbol{\lambda}=(\lambda_1,\ \lambda_2,\ \ldots,\ \lambda_M)$ are introduced for each sample to help bring the approximate solution closer to the nominal solution. Thus, Eq. (16) can be transformed into

$$\|\boldsymbol{f}(\boldsymbol{s}^{\mathrm{CP}})\|_2\le\boldsymbol{\lambda}\varepsilon \tag{17}$$

$\boldsymbol{\lambda}$ may be constructed as a constant vector or a function vector, depending on the needs of the actual application. In this paper, $\boldsymbol{\lambda}$ is constructed in accordance with the distribution of the calibration samples. To avoid touching the proximity sensor or exceeding its measurement range, the sampling rate when the sensor measurement value is in its middle range will be much higher than that when the sensor measurement value is near zero or the maximum range. However, due to the resulting sample imbalance, the basic solution procedure will place too much emphasis on the errors in highly sampled areas and ignore the errors in areas with low sampling rates, resulting in a deviation of the approximate solution from the nominal solution. Thus, the following weight function is employed.

$$\lambda_i=c_k/\max(\boldsymbol{c}),\ i\Rightarrow c_k,\ (i=1,2,...,M;\ k=1,2,...,K) \tag{18}$$

where $c_k$ represents the sample count in the $k$th bin and $\boldsymbol{c}$ represents the vector of the counts $c_k(k=1,2,...,K)$; $K$ is the number of the bins into which the samples are divided. The distribution of the samples is obtained by dividing the samples into $K$ bins in accordance with the sensor measurement values. In addition, $i\Rightarrow c_k$ denotes that the $i$th sample belongs to the $k$th bin. Accordingly, the impact of the unbalanced samples can be reduced by penalizing the samples through Eq. (18).

Then, to effectively apply the weights $\lambda_i$, we need to include the $\lambda_i$ in a new set of constraints as follows:

$$g_i(\boldsymbol{s}^{\mathrm{CP}})=\max\{\|f_i(\boldsymbol{s}^{\mathrm{CP}})\|_2-\lambda_i\varepsilon,0\},\ (i=1,2,...,M) \tag{19}$$

where $g_i(\cdot)$, $(i=1,2,...,M)$ represent the new set of constraints combining Eqs. (17) and (18).

Thus, in terms of sufficiency and necessity, we need only to find a $(\boldsymbol{s}^{\mathrm{CP}})^*$ that satisfies

$$\min_{\boldsymbol{s}^{\mathrm{CP}}}\|\boldsymbol{g}(\boldsymbol{s}^{\mathrm{CP}})\|_2 \tag{20}$$

instead of solving Eq. (17), where $\boldsymbol{g}(\cdot)$ represents the vector of $g_i(\cdot)$ $(i=1,2,...,M)$.

Eq. (20) is a standard optimization problem and is usually solved by optimizing the following equation.

$$\min_{\boldsymbol{s}^{\mathrm{CP}}}\boldsymbol{G}(\boldsymbol{s}^{\mathrm{CP}})=\frac{1}{2}\sum_{i=1}^{M}\left[g_i(\boldsymbol{s}^{\mathrm{CP}})\right]^2=\frac{1}{2}\boldsymbol{g}(\boldsymbol{s}^{\mathrm{CP}})^{\mathrm{T}}\boldsymbol{g}(\boldsymbol{s}^{\mathrm{CP}}) \tag{21}$$

where $\boldsymbol{G}(\cdot)$ represents the ultimate optimization objective derived from Eq. (20).

Finally, the optimal solution can be obtained by applying a commonly used optimization method, such as the Levenberg–Marquardt algorithm.

$$(\boldsymbol{s}^{\mathrm{CP}})^*=\underset{\boldsymbol{s}^{\mathrm{CP}}}{\operatorname{argmin}}\{\boldsymbol{G}(\boldsymbol{s}^{\mathrm{CP}})\} \tag{22}$$

It is worth mentioning that because $\boldsymbol{O}^{\mathrm{CP}}$ and $\boldsymbol{t}^{\mathrm{CP}}$ are the extrinsic parameters of the sensors, the practical meanings of $\boldsymbol{O}^{\mathrm{CP}}$ and $\boldsymbol{t}^{\mathrm{CP}}$ can be considered when solving the problem. The values of $\boldsymbol{O}^{\mathrm{CP}}$, $\boldsymbol{t}^{\mathrm{CP}}$, and $\boldsymbol{s}^{\mathrm{CP}}$ can be roughly estimated by means of measuring equipment, and the solution for $\boldsymbol{s}^{\mathrm{CP}}$ should be near the estimated values of $\boldsymbol{s}^{\mathrm{CP}}$. Moreover, to determine the six extrinsic parameters shown in Eqs. (1) and (2), the calibration plane should be placed in at least five different positions, in accordance with the implicit constraint shown in Eq. (3). Fig. 4 [33] illustrates the calibration process.

### 4.4. Automated control and calibration

A block diagram of the automated calibration system is shown in Fig. 5. Initially, an initial motion control instruction ($l$, $m$, $n$, $\alpha$, $\beta$, $\gamma$) is sent to the automated calibration system. Then, in the actuator module, the 6-DOF motion platform moves the calibration plane to a specific pose according to the motion control instruction. In the measurement module, the proximity sensor produces the measured value of the distance from the proximity sensor to the calibration plane in this specific pose.

Due to the limited measurement range of a proximity sensor, the distance cannot be greater than the maximum range nor less than the safe distance (to avoid bumping the sensor probe). Thus, in the filter module, the pose–distance pairs are filtered to form the calibration datasets. In addition, increments or decrements are employed to adjust the motion control instruction until a sufficient number of samples to form the calibration datasets have been obtained in measurable intervals.

The calibration results are calculated from the datasets in the CPCS, and the results are then transformed into the WCS based

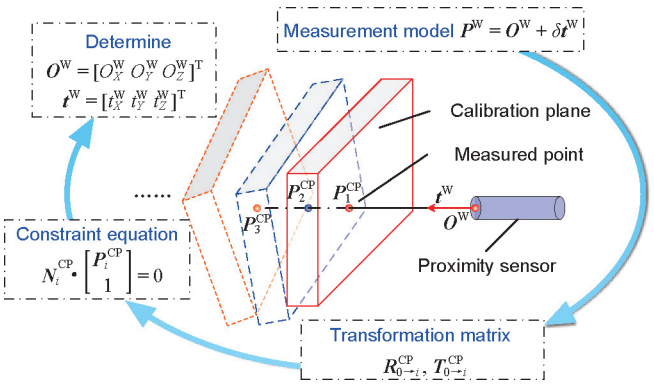


**Fig. 4.** Extrinsic parameter calibration process [33].

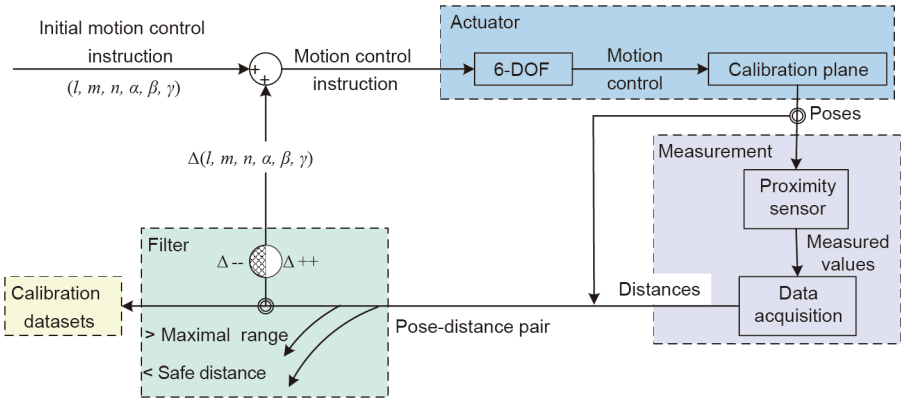


**Fig. 5.** Block diagram of the automated calibration system.

on the coordinates of the datum holes. Thus, the calibration process is finally completed.

## 5. Experiments

In this study, 3D microdisplacement monitoring experiments and *in situ* calibration experiments were carried out (simulation tests were presented in our previous work [33] to verify the feasibility of the proposed method). To verify the accuracy of the proposed calibration and monitoring system, a laboratory system was developed:

(1) To simulate the installation of proximity sensors for the actual measurement of an aircraft assembly tooling system, a fixed measurement frame was designed.

(2) To avoid individual contingency, four proximity sensors (KD2306-4SB, Kaman, USA) were installed on the measurement frame, with a repeatable accuracy within 7 μm in a measurement range of 4 mm.

(3) A calibration plane was prepared from aluminum 6061-T, with a flatness error of less than 3 μm. Then, a high-precision 6-DOF motion platform (H-811.I2, Physik Instrumente, Germany) was employed to apply accurate motion control instructions to the calibration plane, with a repeatability of 3 microradian (μrad) in terms of rotation and 0.15 μm in terms of translation.

(4) Similarly, to facilitate the verification of the system, the 6-DOF motion platform was mounted in a flexible calibration frame to simulate a robot bringing the 6-DOF motion platform and the calibration plane near to a proximity sensor in three orthogonal directions and then locking and holding. Then, the calibration plane was measured in the CPCS with high accuracy, and the installation error could be neglected.

The overall configuration of the instrumentation is shown in Fig. 6 [33].

### 5.1. Laboratory experiments

First, proximity sensors were installed, with their extrinsic parameters as the targets to be calibrated. Pose data of the calibration plane were designed in steps of 0.3° in a range of (−0.6, 0.6)° in terms of rotation and in steps of 0.1 mm in a range of (−1, 1) mm in terms of translation. The values measured by the proximity sensors were obtained by an acquisition module from national instruments (PXI-6289, National Instruments, USA). The whole experimental process was repeated 100 times to test the repeatability. In each calibration test, measured distances were obtained, and their distribution is shown in Fig. 7. In this figure, different colors are employed to distinguish individual calibration tests, and the samples from each calibration test are divided into 20 bins in accordance with the measured values. The horizontal axis represents

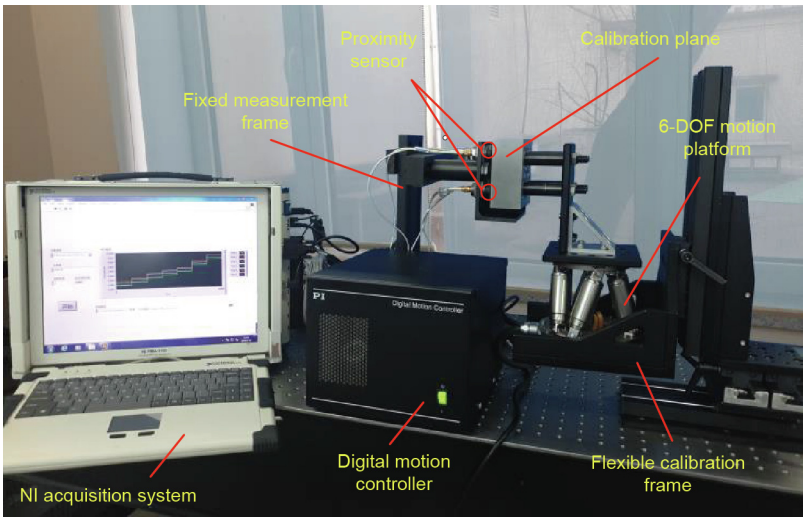


**Fig. 6.** Configuration of the instrumentation in the laboratory [33]. NI: National Instruments.

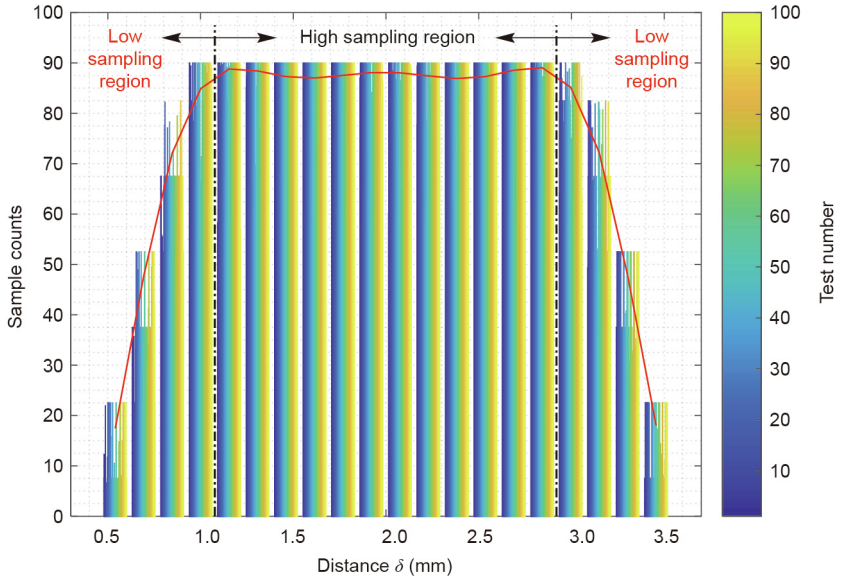


**Fig. 7.** Distribution of displacement measurements.

the different distance bins, and the vertical axis represents the sample counts belonging to each bin in each calibration test. It can be seen that the sampling rates are high and balanced only when the distance values are between approximately 1.15 and 2.85 mm, consistent with the actual use of proximity sensors so as to avoid touching the probe or exceeding the measurement range. However, the difference in the sampling rates between the high and low sampling regions can easily lead to deviations of the calibration results from the nominal values. To solve this problem, the weight function defined in Eq. (18) was adopted.

The calibration results from the laboratory experiments are shown in Table 2.

The experimental results indicate that the calibration process converged. The range of the PBP error fluctuations is less than ±10 μm in the *X* and *Y* directions (in ranges of 900 and 1200 mm, respectively) and ±2 μm in the *Z* direction (in a range of 650 mm), while the range of the UDV error fluctuations is less than 0.07°, thus verifying the stability of the proposed method.

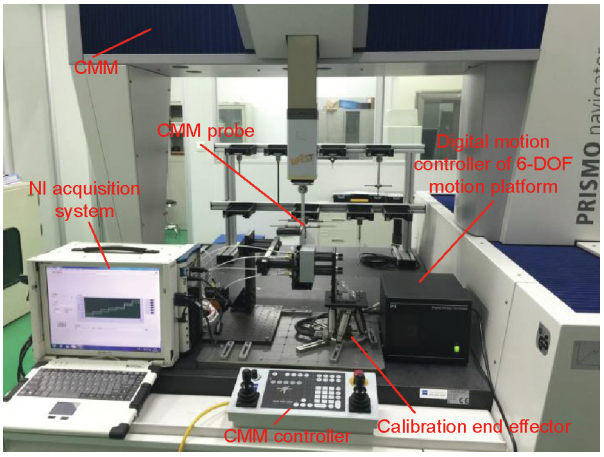


**Fig. 8.** Monitoring accuracy testing system in the laboratory.

### 5.2. Accuracy analysis

Accuracy tests were carried out on a CMM. The layout of the accuracy testing system is shown in Fig. 8. The calibration plane was driven by a 6-DOF motion platform and measured by the CMM to obtain the plane parameters. Based on the calibrated extrinsic parameters of the proximity sensor, the 3D information of the measured points in the measuring plane was obtained, and the projection errors in the measuring plane were calculated to validate the accuracy of the calibration process.

The results based on both weighted and unweighted calibrations are shown in Fig. 9. Consider sensor 1 as an example. After calibration based on unweighted optimization, the measurement errors of the 3D microdisplacements are between −23.50 and 43.30 μm, with the first quartile, median, and third quartile being −12.50, −3.04, and 8.40 μm, respectively. In contrast, after calibration based on weighted optimization, the measurement errors of the 3D microdisplacements are reduced to the relatively small

**Table 2**
Results of the laboratory calibration experiments.

| Parameter (mm) | | Mean | Standard deviation |
|---|---|---|---|
| Pose 1 | $\boldsymbol{O}$ | [18.351 −132.296 131.764] | $10^{-3}$ × [4.99 8.55 1.12] |
| | $\boldsymbol{t}$ | [−0.001 0.307 −0.949] | 0.0373° |
| Pose 2 | $\boldsymbol{O}$ | [−28.151 −135.772 133.268] | $10^{-3}$ × [4.82 8.55 0.79] |
| | $\boldsymbol{t}$ | [−0.031 0.282 −0.955] | 0.0482° |
| Pose 3 | $\boldsymbol{O}$ | [29.461 90.590 132.799] | $10^{-3}$ × [6.38 7.24 0.30] |
| | $\boldsymbol{t}$ | [0.037 0.307 −0.951] | 0.0635° |
| Pose 4 | $\boldsymbol{O}$ | [−19.378 91.536 131.732] | $10^{-3}$ × [4.13 4.97 0.20] |
| | $\boldsymbol{t}$ | [−0.053 0.233 −0.971] | 0.0314° |

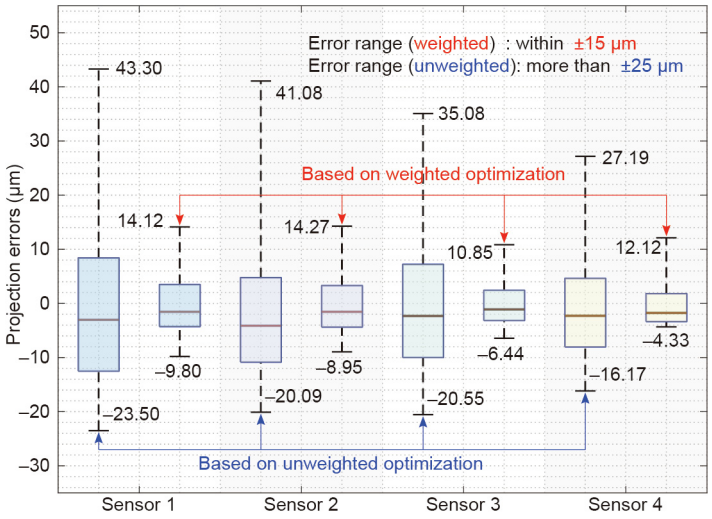


**Fig. 9.** Results of the monitoring accuracy tests.

range between −9.80 and 14.12 μm, with the first quartile, median, and third quartile being −4.27, −1.56, and 3.48 μm, respectively. Thus, it can be seen that the weighted calibration method leads to significant reductions in the measurement errors to within ±15 μm based on the CMM datum (0.90 μm + 2.85 μm·m$^{-1}$ in ranges of 900 mm/1200 mm/650 mm in the *X*/*Y*/*Z* directions). Therefore, the proposed automated calibration method and system can enable high-accuracy spatial measurements.

### 5.3. In situ *calibration and online monitoring*

Calibration and 3D microdisplacement monitoring tests were finally carried out for the process of assembling a tailplane in the laboratory, simulating the process at a production site. The calibration process is depicted in Fig. 10, and the results are shown in Table 3.

After calibration, positioners were installed on the assembly tooling, and their 3D displacements were monitored. In the aircraft assembly process, a spar, actuator and hinge fittings, inner and closing ribs, and lower and upper panels are sequentially assembled, which may lead to progressive increases in gravitational force, artificial thrust, assembly stress, and drilling vibration. Thus, the 3D microdisplacements of the spar positioner (SP), actuator positioner (AP), and hinge positioner (HP) were monitored to ensure high assembly precision and quality. The monitoring process and monitoring system are shown in Fig. 11. Throughout the assembly process, the offset distances off the key positioners (such as SP 1, AP 1, etc.) were acquired by the sensors, and the results are plotted in Fig. 12, where the horizontal axes represent the elapsed time during the assembly process and the vertical axes represent the offset distances of the positioners. The calculated displacements are shown in Table 4.

It can be seen from Fig. 12 that as the aircraft components (such as the spar and actuator) are assembled, the measured distances of the positioners (such as SPs and APs) will oscillate around a value of approximately zero as a result of the vibrations caused by the

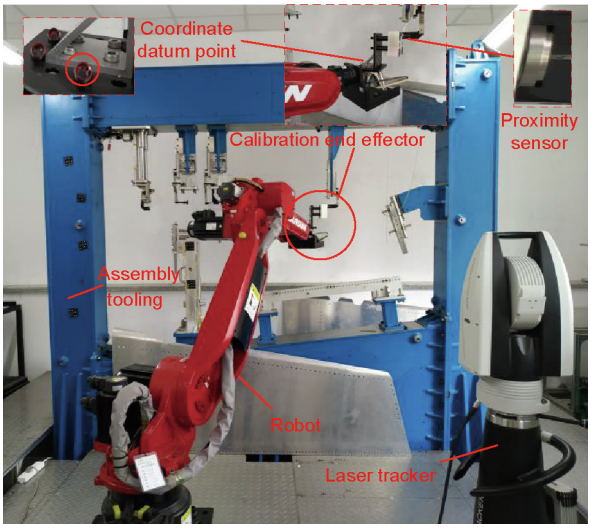


**Fig. 10.** *In situ* calibration system.

**Table 3**
*In situ* calibration results.

| Sensor number | $O_X$ (mm) | $O_Y$ (mm) | $O_Z$ (mm) | $t_X$ | $t_Y$ | $t_Z$ |
|---|---|---|---|---|---|---|
| SP 1 sensor | −1680.845 | −748.645 | 123.805 | −0.028 | 0.910 | −0.414 |
| AP 1 sensor | −1871.246 | −480.598 | 109.775 | 0.326 | −0.197 | −0.925 |
| AP 2 sensor | −1742.015 | −469.605 | 106.003 | −0.116 | 0.993 | 0.021 |
| HP 1 sensor | −1870.849 | −229.299 | 115.794 | 0.007 | −0.210 | −0.978 |
| HP 2 sensor | −1717.989 | −209.531 | 81.399 | 0.279 | 0.946 | −0.163 |
| SP 2 sensor | −1672.594 | 571.228 | 113.139 | 0.080 | 0.992 | −0.096 |

SP: spar positioner; AP: actuator positioner; HP: hinge positioner.

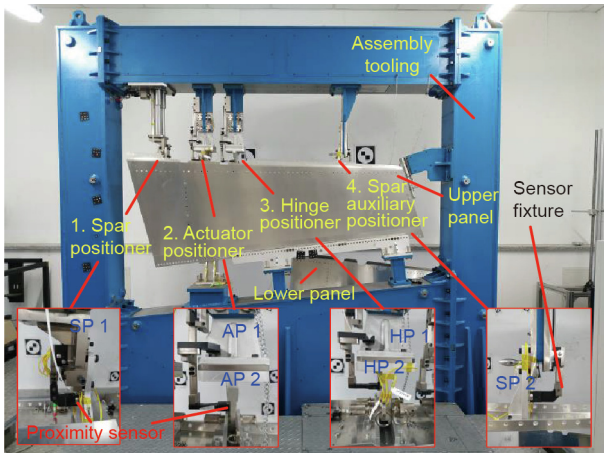


**Fig. 11.** 3D microdisplacement monitoring system during the assembly process.

assembly operations. By adjusting the assembly operations in accordance with the displacement values measured in real time, the amplitudes of the positioner offsets can be controlled within acceptable ranges. In addition, as seen from Table 4, the microdisplacements of the positioners after each assembly step can also be controlled to tiny values to perfectly meet the accuracy requirements of the assembly tooling.

Modern monitoring methods for the assembly process were also tested to compare their efficiency and accuracy at the production site (range of 7 m). As noted previously, a laser tracker was used to collect the datum reference for accuracy assessment in the aircraft assembly process. The accuracy can reach ±57 μm in the range at the production site (7 m) with a laser tracker (AT960, Leica, Germany). However, due to the point-by-point measurement process, the efficiency of the laser tracker is too low to meet the requirements for the online monitoring of 3D microdisplacements. Instead, the industrial photogrammetry method and the 3D microdisplacement monitoring method can be applied for the online monitoring of the assembly tooling because of their high efficiency. To compare its online monitoring accuracy with that of the monitoring method proposed in this paper, an industrial photogrammetry system (MPS/M20, Chenway, China) with an accuracy of ±(14 μm + 14 μm·m$^{-1}$) was adopted. In the range at the production site, the accuracy of this industrial photogrammetry system could reach ±112 μm. Meanwhile, for the method proposed in this paper, a laser tracker (AT960, Leica) was used to establish the WCS, and proximity sensors (KD2306-4SB, Kaman) were used for 3D microdisplacement monitoring. The accuracy was found to reach ±72 μm, including the measurement errors of the 3D microdisplacements (±15 μm) and the errors in the WCS caused by the laser tracker (±57 μm). Thus, the measurement accuracy achieved with the proposed method can perfectly meet the accuracy requirement of ±76 μm for assembly tooling inspection.

In summary, the proposed microdisplacement monitoring method has advantages in both efficiency and accuracy, making it more suitable for online position monitoring during the complex aircraft assembly process. Higher-accuracy monitoring of the microdisplacements can provide better guidance for manual assembly operations, and the online monitoring of microdisplacements will further facilitate aircraft assembly.

## 6. Conclusions

In this paper, a 3D microdisplacement monitoring method based on proximity sensors is presented. An extrinsic parameter calibration method is also proposed and detailed. Laboratory experiments

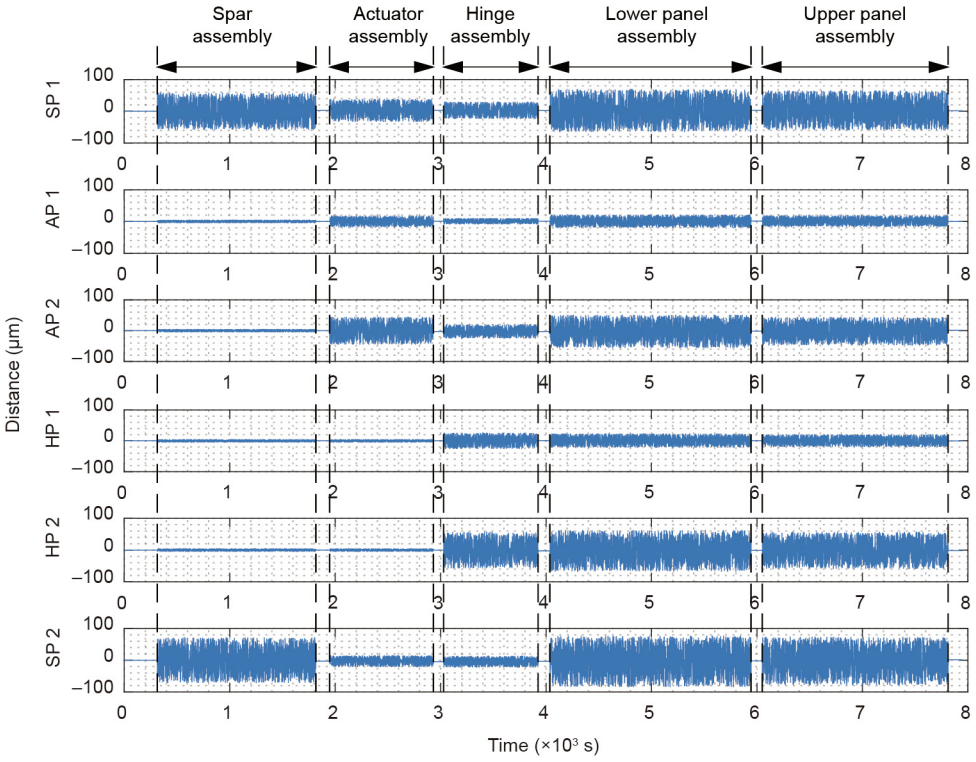


**Fig. 12.** Distance offsets during the assembly process.

**Table 4**
Online monitoring results.

| Assembly process stage | SP 1 (μm) | AP 1 (μm) | AP 2 (μm) | HP 1 (μm) | HP 2 (μm) | SP 2 (μm) |
|---|---|---|---|---|---|---|
| Prework | | | | | | |
| d (Dur.) | 0 | 0 | 0 | 0 | 0 | 0 |
| D (Aft.) | [0 0 0] | [0 0 0] | [0 0 0] | [0 0 0] | [0 0 0] | [0 0 0] |
| Spar | | | | | | |
| d (Dur.) | −57.7–56.2 | −4.4–4.6 | −4.2–4.4 | −3.9–4.8 | −4.7–4.1 | −71.2–69.8 |
| D (Aft.) | [−0.1 2.3 −1.0] | [0 0 0] | [0 0 0] | [0 0 0] | [0 0 0] | [−0.2 −3.1 0.3] |
| Actuator | | | | | | |
| d (Dur.) | −33.1–38.0 | −17.8–18.4 | −44.5–42.3 | −4.5–4.7 | −5.1–3.9 | −20.9–14.6 |
| D (Aft.) | [−0.1 1.6 −0.7] | [−0.2 −0.1 0.6] | [−0.3 2.4 0.1] | [0 0 0] | [0 0 0] | [−0.1 −1.8 0.2] |
| Hinge | | | | | | |
| d (Dur.) | −24.8–28.5 | −9.5–8.2 | −19.8–24.6 | −25.4–25.7 | −56.7–59.2 | −19.6–15.9 |
| D (Aft.) | [−0.1 2.6 −1.2] | [−0.2 0.1 0.6] | [−0.3 2.4 0.1] | [0 −0.1−0.7] | [0.7 2.3 −0.4] | [−0.2 −2.5 0.2] |
| Lower panel | | | | | | |
| d (Dur.) | −63.9–69.5 | −20.7–19.3 | −50.8–55.7 | −21.5–22.9 | −62.6–67.3 | −82.4–77.5 |
| D (Aft.) | [−0.1 1.7 −0.8] | [−0.1 0.1 0.3] | [−0.2 1.7 0] | [0 −0.2 −1.0] | [1.1 3.6 −0.6] | [−0.3 −4.0 0.4] |
| Upper panel | | | | | | |
| d (Dur.) | −60.4–64.2 | −18.0–17.5 | −44.1–47.5 | −19.0–21.0 | −54.0–61.4 | −79.6–71.5 |
| D (Aft.) | [0 1.5 −0.7] | [−0.1 0 0.2] | [0.1 −0.9 0] | [0 0.1 0.5] | [0.4 1.5 −0.3] | [0.1 1.7 −0.2] |

"d (Dur.)" represents the distance measured during the assembly process. "D (Aft.) " represents the microdisplacement after the assembly process.

were conducted using a CMM, and accuracy tests showed that the errors of 3D microdisplacement monitoring can be less than ±15 μm. When the proposed method is applied for *in situ* calibration and online monitoring, the accuracy of 3D microdisplacement monitoring can reach ±72 μm, considering the accuracy of the WCS established based on a laser tracker, which can perfectly meet the accuracy requirements for assembly tooling inspection (±76 μm). The proposed method has been successfully applied for displacement monitoring of the tailplane assembly tooling at a production site, demonstrating that it accurately acquire the displacement of each positioner in real time and provide guidance for subsequent assembly operations. Importantly, 3D displacement monitoring is an indispensable process in manufacturing, testing and many other fields, such as the automobile and ship industries. With its advantages of high precision, fast response and compact volume, the 3D displacement monitoring and calibration method proposed in this paper can effectively support the intelligent manufacturing of aircraft, automobiles, ships, and so forth.

## Acknowledgments

This work was supported in part by the National Natural Science Foundation of China (U1808217), the National Science Fund for Distinguished Young Scholars (52125504), the High-level Personnel Innovation Support Program of Dalian (2017RJ04) and the Liao Ning Revitalization Talents Program (XLYC1807086 and XLYC1801008).

## Compliance with ethics guidelines

Zhenyuan Jia, Bing Liang, Wei Liu, Kun Liu, and Jianwei Ma declare that they have no conflicts of interest or financial conflicts to disclose.

## References

[1] Müller R, Esser M, Vette M. Reconfigurable handling systems as an enabler for large components in mass customized production. J Intell Manuf 2013;24(5):977–90.
[2] McKenna V, Jin Y, Murphy A, Morgan M, Fu R, Qin X, et al. Cost-oriented process optimisation through variation propagation management for aircraft wing spar assembly. Robot Comput Integr Manuf 2019;57:435–51.
[3] Yu L, Zhang Y, Bi Q, Wang Y. Research on surface normal measurement and adjustment in aircraft assembly. Precis Eng 2017;50:482–93.
[4] Deng Z, Huang X, Li S, Xing H. On-line calibration and uncertainties evaluation of spherical joint positions on large aircraft component for zero-clearance posture alignment. Robot Comput Integr Manuf 2019;56:38–54.
[5] Zhong RY, Xu X, Klotz E, Newman ST. Intelligent manufacturing in the context of Industry 4.0: a review. Engineering 2017;3(5):616–30.
[6] Bao Y, Chen Z, Wei S, Xu Y, Tang Z, Li H. The state of the art of data science and engineering in structural health monitoring. Engineering 2019;5(2):234–42.
[7] Chen Z, Du F. Measuring principle and uncertainty analysis of a large volume measurement network based on the combination of iGPS and portable scanner. Measurement 2017;104:263–77.
[8] Hoang VD, Jo KH. A simplified solution to motion estimation using an omnidirectional camera and a 2D LRF sensor. IEEE Trans Ind Inform 2016;12(3):1064–73.
[9] An Yi, Li Bo, Hu H, Zhou X. Building an omnidirectional 3D color laser ranging system through a novel calibration method. IEEE Trans Ind Electron 2019;66(11):8821–31.
[10] Lei P, Zheng L. An automated *in situ* alignment approach for finish machining assembly interfaces of large-scale components. Robot Comput Integr Manuf 2017;46:130–43.
[11] Pérez Muñoz P, Albajez García JA, Santolaria Mazo J. Analysis of the initial thermal stabilization and air turbulences effects on laser tracker measurements. J Manuf Syst 2016;41:277–86.
[12] Schmitt RH, Peterek M, Morse E, Knapp W, Galetto M, Härtig F, et al. Advances in large-scale metrology—review and future trends. CIRP Ann 2016;65(2):643–65.
[13] Li X, Li X, Ge SS, Khyam MO, Luo C. Automatic welding seam tracking and identification. IEEE Trans Ind Electron 2017;64(9):7261–71.
[14] Wang Z. An imaging and measurement system for robust reconstruction of weld pool during arc welding. IEEE Trans Ind Electron 2015;62(8):5109–18.
[15] Spencer BF, Hoskere V, Narazaki Y. Advances in computer vision-based civil infrastructure inspection and monitoring. Engineering 2019;5(2):199–222.
[16] Lee T, Kim C, Cho DD. A monocular vision sensor-based efficient SLAM method for indoor service robots. IEEE Trans Ind Electron 2019;66(1):318–28.
[17] Xu Y, Gao F, Jiang X. Performance analysis and evaluation of geometric parameters in stereo deflectometry. Engineering 2018;4(6):806–15.
[18] Cervera A, Ezra O, Kuperman A, Peretz MM. Modeling and control of magnetic actuation systems based on sensorless displacement information. IEEE Trans Ind Electron 2019;66(6):4849–59.
[19] Caetano DM, Rabuske T, Fernandes J, Pelkner M, Fermon C, Cardoso S, et al. High-resolution nondestructive test probes based on magnetoresistive sensors. IEEE Trans Ind Electron 2019;66(9):7326–37.
[20] Peng K, Yu Z, Liu X, Chen Z, Pu H. Features of capacitive displacement sensing that provide high-accuracy measurements with reduced manufacturing precision. IEEE Trans Ind Electron 2017;64(9):7377–86.
[21] Uekita M, Takaya Y. On-machine dimensional measurement of large parts by compensating for volumetric errors of machine tools. Precis Eng 2016;43:200–10.
[22] Kim YK, Kim KS, Kim S. A portable and remote 6-DOF pose sensor system with a long measurement range based on 1-D laser sensors. IEEE Trans Ind Electron 2015;62(9):5722–9.
[23] Liu S, Xu De, Zhang D, Zhang Z. High precision automatic assembly based on microscopic vision and force information. IEEE Trans Autom Sci Eng 2016;13(1):382–93.
[24] Kim YK, Kim Y, Jung YS, Jang IG, Kim KS, Kim S, et al. Developing accurate long-distance 6-DOF motion detection with one-dimensional laser sensors: three-beam detection system. IEEE Trans Ind Electron 2013;60(8):3386–95.

[25] Zapico P, Fernández P, Rico JC, Valiño G, Patiño H. Extrinsic calibration of a conoscopic holography system integrated in a CMM. Precis Eng 2018;52:484–93.
[26] Liu W, Wang T, Liang B, Feng Di, Jiang X, Zhang Y, et al. Measurement of three-dimensional information by single eddy current displacement sensor. IEEE Sens J 2019;19(9):3543–52.
[27] Bi C, Fang J, Li K, Guo Z. Extrinsic calibration of a laser displacement sensor in a non-contact coordinate measuring machine. Chin J Aeronaut 2017;30 (4):1528–37.
[28] Bi C, Liu Y, Fang J, Guo X, Lv L, Dong P. Calibration of laser beam direction for optical coordinate measuring system. Measurement 2015;73:191–9.
[29] Wu L, Ren H. Finding the kinematic base frame of a robot by hand–eye calibration using 3D position data. IEEE Trans Autom Sci Eng 2017;14 (1):314–24.
[30] Guo Y, Song B, Tang X, Zhou X, Jiang Z. A measurement method for calibrating kinematic parameters of industrial robots with point constraint by a laser displacement sensor. Meas Sci Technol 2020;31(7):075004.
[31] Sharifzadeh S, Biro I, Kinnell P. Robust hand–eye calibration of 2D laser sensors using a single-plane calibration artefact. Robot Comput Integr Manuf 2020;61:101823.
[32] Zou Y, Lan R. An end-to-end calibration method for welding robot laser vision systems with deep reinforcement learning. IEEE Trans Instrum Meas 2020;69 (7):4270–80.
[33] Liang B, Liu W, Jiang X, Feng D, Liu K, Zhou M, et al. A novel automatic calibration method for displacement sensors based on the spatial transformation theory. In: Proceedings of 2019 IEEE/ASME International Conference on Advanced Intelligent Mechatronics; 2019 Jul 8–12; Hong Kong, China; 2019.